https://doi.org/10.1016/j.jpowsour.2021.229979

In-situ introducing TiP_2 nanocrystals in black phosphorus anode to promote high rate-capacity synergy

Fengchen Zhou[a], Xu-Sheng Yang[c,d*], Jiangwen Liu[a], Jun Liu[a], Renzong Hu[a], Liuzhang Ouyang[a,b**], Min Zhu[a]

[a] School of Materials Science and Engineering, Guangdong Provincial Key Laboratory of Advanced Energy Storage Materials, South China University of Technology, Guangzhou, 510641, China. Email: meouyang@scut.edu.cn

[b] China-Australia Joint Laboratory for Energy & Environmental Materials, Key Laboratory of Fuel Cell Technology of Guangdong Province, Guangzhou, 510641, China

[c] Advanced Manufacturing Technology Research Centre, Department of Industrial and Systems Engineering, The Hong Kong Polytechnic University, Hung Hom, Kowloon, Hong Kong, China. Email: xsyang@polyu.edu.hk

[d] Hong Kong Polytechnic University Shenzhen Research Institute, Shenzhen 518057, China

[*]Corresponding authors.
[a**] E-mail: meouyang@scut.edu.cn, (L. Ouyang)

[c*] E-mail: xsyang@polyu.edu.hk, (X. Yang)

Abstract：

Owing to the high theoretic capacity (2596 mAh g^{-1}) and suitable lithiation potential (~ 0.7 V vs. Li^+/Li), Black phosphorus (BP) is considered as an ideal anode material for the fast-charging lithium-ion batteries. However, BP still faces the large volume change and low Li^+ transfer during the charge/discharge. In this work, a facile two-step high-energy ball milling method is developed to synthesis the black phosphorus@TiP_2-C (CBP@TiP_2-C) nanocomposite for the high-rate performance anode material, in which the conductive nanocrystalline TiP_2 is *in-situ* introduced into BP matrix. We reveal that the uniformly dispersed TiP_2 nanocrystals can enhance the electronic and ionic conductivities of active particles and the electrode reaction kinetics. The lithiation product cubic Li_yTiP_4 phase is beneficial to release the stress, reduce the Li^+ diffusion energy barrier and accelerate the Li^+ extraction from LiP_3 upon delithiation. Moreover, the contact among different components can be improved by Ti-C and P-C bonds in the CBP@TiP_2-C, thus ensuring excellent electric contact within the material and enhancing the structural stability of composites. As a result, the CBP@TiP_2-C anode displays a high reversible capacity of 1007.4 mAh g^{-1} at 10.0 A g^{-1} and excellent capacity retention of 925.6 mAh g^{-1} after 500 cycles at 2 A g^{-1}.

Key words: TiP_2 nanocrystal, black phosphorus, *in-situ*, chemical bond, lithium ion battery

Introduction

Lithium-ion batteries (LIBs) have been an important part of the mobile electronics revolution for improving our lives since last two decades. Today, more important discoveries are expected to advance battery technology, and the lower specific capacity of commercial graphite has promoted many alternative materials.[1, 2] Among the various potential anode materials for the fast-charging LIBs, Phosphorus exhibits both high theoretic capacity (2596 mAh g^{-1}) and suitable lithiation potential (~ 0.7 V vs. Li^+/Li).[3-5] However, phosphorus still faces the large volume change and obvious fading rate-capacity during the electrochemical process, showing the poor characteristic of stabilization.

Some common strategies, including spatial confinement method [4-7] and nano-sizing effect [8-10], have been adopted to address the volume change during the cycling process. Although it has promise in terms of cyclic stability to a certain extent, the rate performance is still needed to improve to meet the real fast-charging application. It has been noted that introducing one material with high ion migration and small volume change into composites is an effective strategy to stabilize the electrochemical property of electrode materials.[11, 12] The introduced material would not only enhance the ionic conductivity of composite, but also buffer the stress of volume expansion, thereby resulting in the improved electrochemical cycling properties and rate performance. For example, our previous work has demonstrated that introducing TiO_2 into black phosphorus (BP)-C composites can relieve the stress of volume expansion and enhance the Li^+ migration kinetic, resulting in an excellent cycle retention and rate

capabilities.[12] However, the relatively high Li^+ insertion/extraction potential of TiO_2 (i.e. 1.75/2.05 V) has no contribution of capacity between the 0.01-2.00 V (vs. Li^+/Li) potential window, which reduces the capacity of the composites.

Transition metal phosphides (TMPs) with high conductivity and electrochemical activity have been considered as promising additive material to stabilize the electrochemical performance of P-based electrode.[13-17] Besides, TMPs can be easily scaled up through transition metal and red phosphorus with a cost-effective and simple mechanical ball milling technology. Thus, a one-step ball milling process can be used to *in-situ* synthesize BP-TMPs composite.[18] The *in-situ* formed TMPs can facilitate the contact between BP and ultra-fast electronic transport, and modify the edge-atom of BP to ensure the open edges for fast Li^+ entry.[19] Among the TMPs, it has been found that the intercalation-type metal phosphides are generally showing impressive low volume change and fast Li^+ migration kinetics.[20-23] For instance, titanium-based phosphide can form a stable Li-Ti-P phase with a reversible fast insertion/extraction of Li^+ from the host matrix during the discharge/charge process.[22, 24] In particular, Kim et al. has recently confirmed that introducing crystalline TiP_2 into red P-C system can improve the cycling performance due to the structural reinforcement by forming a stable Li_yTiP_4 active matrix during lithiation.[25] However, the improved cycling performance and rate capacity in TiP_2-red P-C composite system is still considered to be less-than-practical.

Herein, a two-step ball milling process is developed to first *in-situ* synthesize black phosphorus@TiP_2 (CBP@TiP_2) composites, and then fabricate CBP@TiP_2-C

composites with expanded graphite (EG). With the *in-situ* process, uniformly dispersed TiP_2 nanocrystal can facilitate contact between BP and ultra-fast electronic transport, and modify the edge-atom of BP to ensure open edges for fast Li^+ entry. Besides, the TiP_2 can also be used as a buffer material to release the large volume expansion of BP during cycling. In addition, the formed chemical bonds of Ti-C and P-C further improved the connections between different components, thereby promoting the electronic conductivity and structural stability of the composites. As a result, the *in-situ* formed CBP@TiP_2-C composite demonstrates a superior stable lithium storage performance and excellent rate capacities, e.g., even after 500 cycles at 2 A g^{-1}, a high reversible capacity of 925.6 mAh g^{-1} is obtained with capacity retention of 79.8%.

2. Experimental

2.1 Material preparation

Commercial red P (Aladdin) was ball milled in deionized (DI) water by using a planetary milling equipment (QM-3SP4, Nanjing Nada Instrument Co. Ltd.) that was operated at 400 rpm for 10 h to obtain the refined red phosphorus particles. Then, the dispersion mixture was transferred into an autoclave, and heated at 180 °C for 10 h to further mitigate the surface oxidation. After hydrothermal reaction, the purified red P was obtained after centrifuged and vacuum-dried. Expanded graphite (EG) was obtained by heating the expandable graphite (Qingdao Xinghua Co., Ltd.) for 2 minutes at 950 °C in a furnace under an air atmosphere.

The two-step ball milling process for in-situ synthesizing CBP@TiP_2-C nanocomposites is described as follows. Firstly, the purified red P and Ti powder

(Aladdin) with a molar ratio of 6:1 were ball milled by high-energy shaking ball milling equipment (QM-3C, Nanjing Nada Instrument Co. Ltd.) for 2h to obtain CBP@TiP_2. Then, the obtained CBP@TiP_2 was mixed with EG at 7:3 wt% and shaking ball milled for another 10 h to obtain CBP@TiP_2-C nanocomposites. The ball-to-powder ratio was 50:1 with a ball milling rotation rate of 1200 rpm under Argon atmosphere. For comparison, the CBP-C composite was also prepared with a BP and EG weight ratio of 7:3 under the same milling conditions. In comparison with the CBP@TiP2-C composite, another similar composite, namely BP@TiP_2-C composite, was also synthesized with the same methods, only without the ball milling process of red P as raw material. While, CBP-TiP_2-C composite was synthesized using BP, EG and Ti power by one-step ball milling. BP was prepared by ball milling disposed red P for 2h with shaking ball milling equipment.

2.2 Material characterization

X-ray diffraction patterns (XRD) were obtained by Cu Kα radiation (PANalytical Empyrean) to identify the phase constitutes of the samples. X-ray photoelectron spectroscopy (XPS) spectra was collected by Thermo Scientific ESCALAB 250. The morphologies and the detailed microstructures were analyzed by scanning electron microscopy (SEM, Carl Zeiss Supra 40) and transmission electron microscopy (TEM, JEOL JEM-2100) operating at the voltage of 200 kV.

2.3 Electrochemical characterization

The electrode was fabricated by mixing active material (70 wt%), carboxymethyl cellulose (15 wt%) and Super P (15 wt%) in DI water, coating on a copper foil and

drying overnight at 100 °C under vacuum condition. The active material loading density was ~0.8 mg cm^{-2}. The test cells were assembled with lithium foils as the counter electrode in an argon-filled glove box. Electrolyte was 1 M $LiPF_6$ into a mixture of EC/DEC/DMC (1/1/1, v/v/v) with the addition of 10 wt% FEC. A battery test system (LAND CT2001A) was used to conduct the charge-discharge test with 0.01-2.00 V (vs. Li^+/Li) voltage window. The current densities and the specific capacities were calculated according to the weight of composites. Electrochemical impedance spectroscopy (EIS, frequency between 100 kHz to 0.01 Hz) and cyclic voltammetry (CV, voltage window between 0.01-2.00 V) curves were measured on electrochemistry workstation (Gamry Interface 1000). The SEM and TEM specimens of cycled electrodes were prepared by disassembling the test cells, cleaning with DEC and drying in the glove box.

3. Results and discussion

3.1 Structure and morphology

The XRD patterns are firstly obtained in Fig. 1a to identify the phase structure of synthesized materials. Fig. 1a shows that the Ti powder and disposed red P are respectively transformed into black P and TiP_2 for forming the CBP@TiP_2 composite during the ball milling process, which can be well-accorded with the corresponding standard patterns JCPDS NO. 73-1358 and NO. 73-1835. Fig. 1a also shows the XRD pattern of CBP@TiP_2-C composite, which was synthesized by further ball milling CBP@TiP_2 with EG. On one hand, it demonstrates that the diffraction peaks of BP almost disappear except for one weak peak located at 35°. On the other hand, only the

characteristic peaks of TiP_2 and a weaker peak of carbon located at 26.5° can be indexed in CBP@TiP_2-C composite, indicating that there is no reaction between CBP@TiP_2 and EG. For comparison, red P without pre-ball milling is also used as raw material to synthesize BP@TiP_2 and BP@TiP_2-C (corresponding XRD patterns can be found in Fig. S1). Comparing with the BP@TiP_2 composite, it shows that the diffraction peaks of TiP_2 in the CBP@TiP_2-C composite prepared by red P with ball milled is significantly widened and weakened. Based on the Scherrer equation, the corresponding gran size of TiP_2 in CBP@TiP_2-C composite is smaller than that in BP@TiP_2.[36] The smaller grain size is favorable for the uniform dispersion in BP matrix and shortening the Li^+ diffusion path. The XRD patterns of samples without Ti powder addition, i.e., CBP and CBP-C composites, are also given in Fig. S3a. It can be observed that the characteristic diffraction peaks of the disposed red P are transformed into black P during the ball milling process, which is not disappeared but only weaken in CBP-C after further ball milled with EG.

Fig. 1b-d gives the SEM images of disposed red P, CBP@TiP_2, and CBP@TiP_2-C, respectively. After the ball milling process, the original size of disposed red P has significantly reduced from several tens of micron (as shown in Fig. S2b) to 1-3 μm as shown in Fig. 1b. In contrast to the large size, the small-size phosphorus should have a shorter Li+ diffusion path in the phosphorus particle, which would be significantly less time-consuming during the lithium extraction process. In this regards, it can improve the extraction reversibility of Li from Li-P phase and avoid the lithium trapping in the electrode, thus enhancing the capacity retention of phosphorus.[26, 27] Fig. 1c shows

the SEM image of CBP@TiP_2, which has a uniform distribution at the nanometer scale. Moreover, the TEM image of CBP@TiP_2 shows that the TiP_2 was in-situ introduced and embedded into BP matrix, as shown in Fig. S2d. After the CBP@TiP_2 is ball milled with EG, Fig. 1d shows that the synthesized CBP@TiP_2-C composite also has a uniform size distribution at the nanometer scale, except for few micro-sized particles. In contrast, the undisposed red P-synthesized BP@TiP_2 and BP@TiP_2-C composites have obvious larger size distribution with some particle even over ~10 μm, as shown in Fig. S1c and d. Noticeably, CBP@TiP_2-C with smaller and more uniform particle distribution would shorten the diffusion path of lithium ion, thus further improving the kinetics of the electrochemical reaction. In addition, Fig. S3b shows the SEM image of CBP-C composite, which exhibits a micro-sized secondary granular structure composed of high-density nano-sized primary particles.

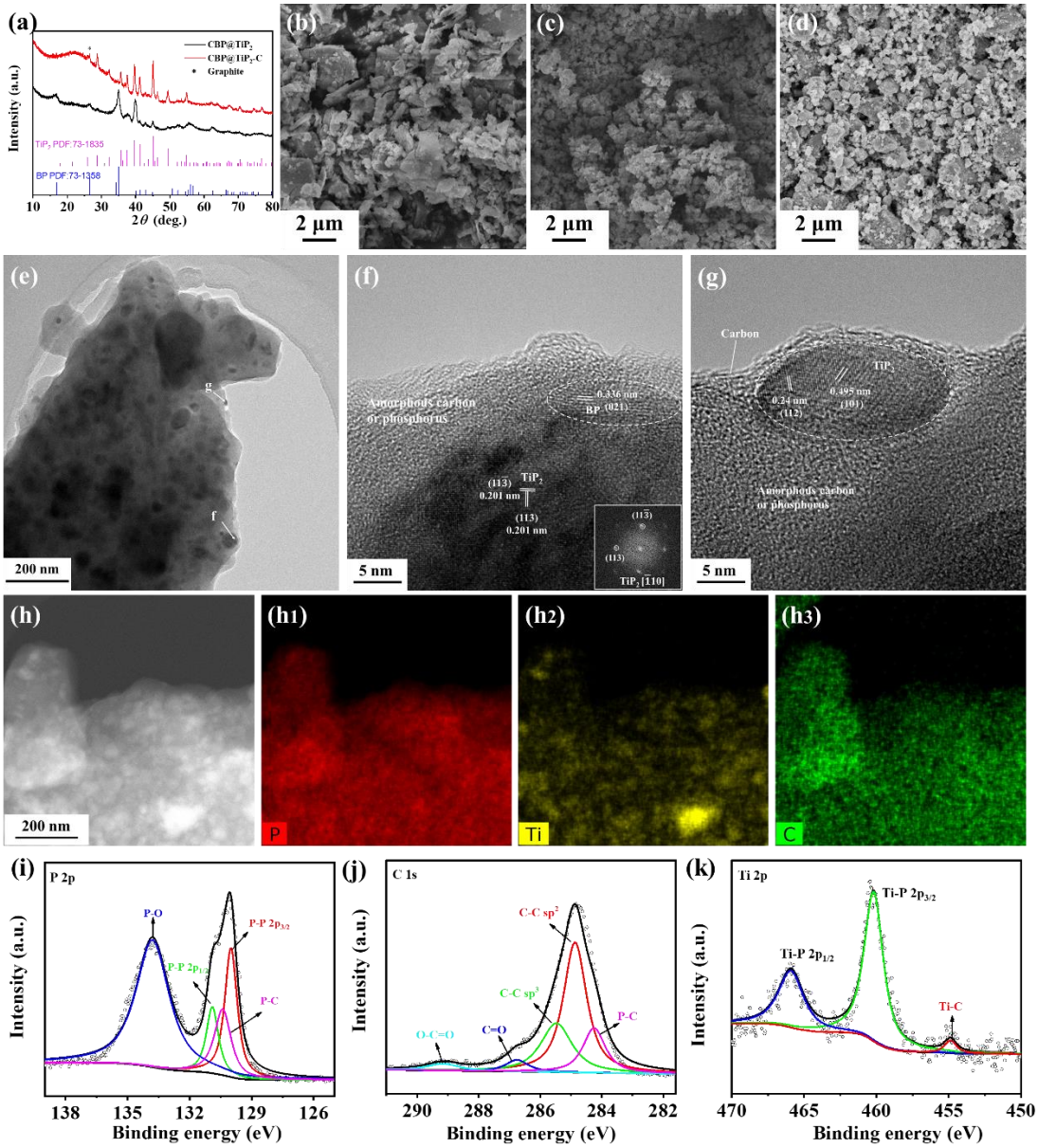

Fig. 1 a) The XRD patterns of CBP@TiP_2 and CBP@TiP_2-C composites. The SEM images of b) disposed red P, c) CBP@TiP_2, and d) CBP@TiP_2-C. e) TEM image of CBP@TiP_2-C, f) HRTEM image of the f region in (e), g) HRTEM image of the g region in (e), h) scanning TEM (STEM) image of (e), h1-h3) the element mapping images in (h). High-resolution XPS spectrum of i) P 2p, j) C 1s, and k) Ti 2p of CBP@TiP_2-C composite.

TEM and HRTEM (Fig. 1e-g) images are used to investigate the detailed morphology and structure of CBP@TiP_2-C composite. After the second ball milling step, Fig. 1e shows that the nano-sized TiP_2 crystalline particles (dark particle area) pre-formed in the first ball milling step are finally uniformly distributed in BP-C matrix. Fig. 1f and

Fig. 1g show HRTEM images enlarged from the regions (f) and (g) in Fig. 1e, respectively. The lattice spacing corresponded to the different planes of TiP_2 are well-indexed in Fig. 1f-g to further confirm the existence of TiP_2 nanocrystalline particles. Besides, it should be noted that there is also a lattice fringe with *d*-spacing of 0.34 nm in Fig. 1f, which relates to (021) plane of BP. Fig. 1f also shows that a few carbon layers coated on surface of the nanocomposite. Fig. 1h1-h3 shows the elemental mapping analysis of CBP@TiP_2-C based on Fig. 1h, which exhibits the homogeneous distribution of P and C elements. Moreover, the distribution of Ti element is similar to the dark particle area in Fig. 1e, further confirming that the dark particle area in Fig. 1e is ascribe to TiP_2 crystals. In contrast, no obvious lattice spacing can be indexed in the surface regions in Fig. 1f and g, which only exist P and C elements according to the elemental mapping results. Therefore, it should be amorphous C and P regions, as signed in Fig. 1f and g, which should be resulted from the high-energy ball milling process. HRTEM images of CBP-C composites are also given in Fig. S3c-d, in which the graphite sheets are pulverized into basic structural units (BSUs), and the BP is also existed according to the corresponding lattice fringes indexed in the figure.[28] The above observed results indicate that the two-step ball milling synthesis process leads to the uniform distribution of TiP_2 uniform in BP-C matrix in CBP@TiP_2-C nanocomposite, which might be able to contribute to the electronic/ionic transferring and release the stress for the volume expansion of BP. In addition, the outer carbon layer can avoid the direct contact between BP and TiP_2 with electrolyte to stabilize solid electrolyte interface.[37, 38]

In addition, Fig. 1i-k show respectively the P 2p, C 1s and Ti 2p XPS spectrums of the CBP@TiP_2-C composites. The P 2p XPS spectrum can be deconvoluted into four peaks in Fig. 1i, in which the peaks located around 129.8 eV and 130.7 eV are corresponded to the pair $2p_{3/2}$ and $2p_{1/2}$ of P-P bond, respectively.[29, 30] While, the peak located at 130.2 eV can be ascribed to P-C bond. It is worth noting that the P-C bond can enhance the contact between BP and C, thus ensuring the electrical contact between BP and C during the lithiation/delithiation.[29] In addition, the peak appeared at 133.8 eV is attributed to the P-O bond, as shown in Fig. 1i, which should be attributed to the slight oxidation of composites exposed in air. Interestingly, other peaks related to TiP_2 phase are not found, in contrast to that in CBP-C composites (Fig. S4a), due to the possible overlapping by the pure phosphorus.[25] Fig.1j shows that the C 1s spectrum can be fitted into five peaks located at 284.2 eV (C-P bond), 284.8 eV (sp^2 C-C bond), 285.6 eV (sp^3 C-C bond), 286.8 eV (C=O bond), and 289.2 eV (O-C=O bond), respectively.[29-31] Three peaks can be fitted in Ti 2p spectrum, as shown in Fig. 1k. More specifically, a pair peaks located at 460.2 eV and 465.9 eV are corresponded to the $2p_{3/2}$ and $2p_{1/2}$ of Ti-P bonds, respectively. While, a weak peak appeared at 454.9 eV can be corresponded to Ti-C bond.[32] The chemical bonds between BP, TiP_2 and C can efficiently improve the contact among different components within the material and enhance the structural stability of composites.

3.2 Electrochemical performance characterization

To evaluate the electrochemical performance of the CBP@TiP_2-C nanocomposite, lithium ion half batteries are assembled and conducted with 0.01-2.00 V (vs. Li^+/Li)

voltage window. Fig. 2a shows the initial and second charge/discharge profiles of CBP@TiP_2-C and CBP-C electrodes at 500 mA g^{-1}. Both electrodes exhibit two sloping profiles located at 0.5-0.9 V upon discharge process and 1.0-1.2 V upon the charge process, which is corresponded to the typical lithiation/delithiation process of phosphorus. However, the discharge voltage of CBP@TiP_2-C is lower than that of CBP-C, indicating the larger polarization phenomena of the CBP@TiP_2-C electrode. Based on the EIS result of uncycled electrodes (as shown in Fig. S5), the CBP@TiP_2-C electrode has a large resistance than that of CBP-C electrode. This might be due to the smaller particles that leads to the voids in CBP@TiP_2-C electrode plate. With the expansion of particles after the discharge, these voids would be filled to ensure the effective inter-contact and subsequently enhance the electrochemical property of CBP@TiP_2-C electrode. Accordingly, the CBP@TiP_2-C electrode can deliver an initial discharge specific capacity of 1682.1 mAh g^{-1} with initial coulombic efficiency (ICE) of 87.6%, as indicated in Fig. 2a. These results are lower than that of CBP-C electrode due to the high content of BP in CBP-C composite, the lithium inserted into TiP_2 (Li_yTiP_4, $y < 11$) can be incompletely extracted, and the small size of CBP@TiP_2-C expose more contact area with electrolyte results more side reaction. During the second cycle, the coulombic efficiency of CBP@TiP_2-C electrode can increase to 98.6%. To further investigate the lithiation mechanisms, CV curves of CBP@TiP_2-C and CBP-C are delivered and compared in Fig. 2b-c with the same scan rate of 0.1 mV s^{-1}. During the initial cathodic scan of CBP@TiP_2-C electrode, as shown in Fig. 2b, a peak appeared at 0.5 V is corresponded to the formation of Li_xP ($x = 1$-3) and Li_yTiP_4 by

inserting the lithium into BP and TiP_2.[23, 33] Besides, an obvious peak at 1.0 V and a weak peak at 1.2 V during the anodic scan can be ascribed to the delithiation process. The well-repeated CV curves in the follow-up cycles in Fig. 2b indicates the excellent reversibility in electrochemical reaction of CBP@TiP_2-C electrode. In contrast, the CV curves of CBP-C show some differences (Fig. 2c). First, there is an extra peak appeared at 1.05 V in the initial cathodic scan, which attributes to the formation of solid electrolyte interface (SEI). Moreover, the cathodic peak at 0.6 V is splinted into two peaks, *ca.* 0.55 and 0.7 V, in the subsequent cycles, demonstrating the stepwise lithiation process of BP due to the slow ionic diffusion. More importantly, in addition to the anodic peak of located at 1.0 V, there is another obvious peak appeared at 1.2 V of CBP-C, demonstrating the higher polarization of the electrode. These results indicate that TiP_2 introduction can improve the ionic and electronic conductivity, thus simultaneously reducing the polarization and accelerating the extraction of Li^+ during the charging process.

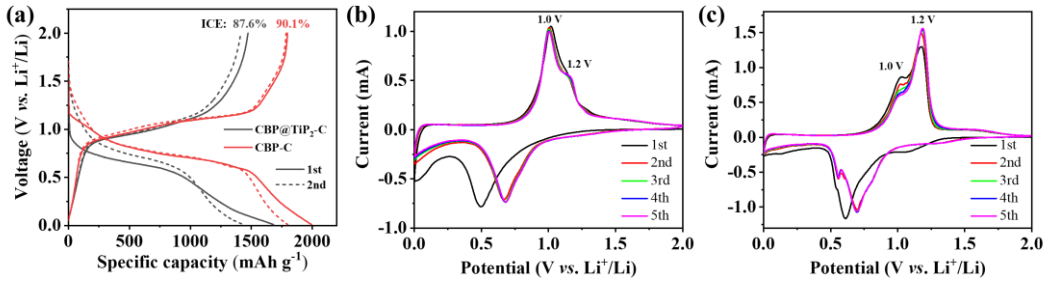

Fig. 2 a) The initial and second voltage profiles of CBP@TiP_2-C and CBP-C at 500 mA g^{-1}. The CV curves of b) CBP@TiP_2-C and c) CBP-C at a scan rate of 0.1 mV s^{-1}.

Fig. 3a shows the cyclic performance and columbic efficiencies of CBP@TiP_2-C and CBP-C electrodes at the current density of 500 mA g^{-1}. The CBP@TiP_2-C electrode

demonstrates a distinct capacity fading during the initial several cycles. However, the cyclic electrochemical performance of CBP@TiP_2-C electrode becomes stable after *ca.* 10 cycles, denoting a reversible specific capacity of 1124.1 mAh g^{-1} and capacity retention of 76.4% after 300 cycles. In contrast, the cyclic performance of CBP-C electrode shows a continuous fading, only maintaining a revisable capacity of 1007.8 mAh g^{-1} with a capacity retention of 56.1% after 300 cycles. Additionally, the coulombic efficiency of CBP@TiP_2-C can achieve 99.5% after the initial five cycles and maintain at 99.65% upon cycles, higher than that of CBP-C electrode with more side-reaction occurring and irreversible lithium trapping. The significantly improved cyclic performance of CBP@TiP_2-C electrode may be attributed to the formation of stable cubic Li_yTiP_4 phase upon cycling that can act as a buffer matrix to absorb the stress caused by Li_xP. Specifically, it has been reported that the volume change with the variation of lithium content in the Li_yTiP_4 phase (y = 6.5-10.5) is less than 1%.[22, 23] To further examine the structural evolution, the morphologies of two electrodes before and after cycling are examined by SEM (Fig. S6). It shows that the CBP@TiP_2-C electrode can maintain the structural integrity during the cycling, with the active material remaining close electrical contact. In contrast, the surface of the CBP-C electrode after cycling shows numerous cracks, which will expose more electrolyte/electrode active interfaces, thus accelerating the electrolyte decomposition. Moreover, the cross-sectional image of the CBP@TiP_2-C electrode shows the less volume expansion than that of CBP-C electrode. These results clearly demonstrate the CBP@TiP_2-C composite has excellent capability to alleviate the volume change during

the electrochemical process.

Fig. 3b shows the rate performance of CBP@TiP_2-C and CBP-C electrodes at different current densities. The CBP@TiP_2-C electrode can exhibit the average specific capacities of 1345.8, 1236.7, 1185.0, 1138.6, 1108.7, 1071.8 and 1044.8 mAh g^{-1} at current densities of 0.2, 0.5,1.0, 2.0, 3.0, 5.0 and 7.0 A g^{-1}, respectively. Even at a high current density of 10.0 A g^{-1}, the corresponding average specific capacity can still be maintained at 1007.4 mAh g^{-1}, with a capacity retention of 74.9% calculated based on the capacity at 0.2 A g^{-1}. The rate performance of the CBP@TiP_2-C is better than that of reported P-TiP_2-C composites with a capacity of 919 mAh g^{-1} at 3.2 A g^{-1}.[25] It is noted that, due to the higher P content, the CBP-C electrode exhibits higher capacities than that of the CBP@TiP_2-C at relatively low current densities between 0.2-5.0 A g^{-1}. However, the fading rate of the specific capacity with increasing current density in CBP-C electrode is obviously faster than that of the CBP@TiP_2-C electrode, e.g., leading to a lower capacity of 827.9 mAh g^{-1} in the CBP-C electrode than that of 1050 mAh g^{-1} in the CBP@TiP_2-C electrode at 10 A g^{-1}. It indicates the inferior Li^+ diffusion in CBP-C composite. More impressively, the CBP@TiP_2-C electrode can achieve a high capacity of 1196.8 mAh g^{-1} once returning to 0.5 A g^{-1} after ultrahigh rate cycling, and stable cycling for another follow-up 50 cycles without obviously fading, demonstrating an excellent rate performance. Compared with the P-based composites in literature, the prepared CBP@TiP_2-C electrode in the present work shows excellent rate capability and high specific capacity, as presented in Table S1. The improvement of rate performance in the CBP@TiP_2-C composite should be benefited from the

uniform distribution of the conductive TiP_2 nanocrystals in BP matrix, which can effectively enhance the ionic/electronic conductivity, thus facilitating the Li^+ migration during the fast charge/discharge process. Moreover, the chemical bonds in the *in-situ* synthesized CBP@TiP_2-C composite can strengthen the contact among different components, thus ensuring the excellent electric contact, and enhancing the structural stability of composites.

The long-term cycling performance at the higher current density of 2000 mA g^{-1} of the CBP@TiP_2-C and CBP-C composites are also evaluated and compared, as shown in Fig. 3c. More specifically, a high capacity of ~925.6 mAh g^{-1} with 79.8% capacity retention (calculation is based on the 4^{th} cycle) and columbic efficiency of 99.84% can be obtained in the CBP@TiP_2-C electrode after 500 cycles. In contrast, the CBP-C electrode can only show a lower capacity of 681.3 mAh g^{-1} after 500 cycles. For comparison, the cycling property of the BP@TiP_2-C and CBP-TiP_2-C electrodes are investigated (Fig. S7), which shows that the BP@TiP_2-C electrode demonstrates the almost same cyclic capacity as that of CBP@TiP_2-C electrode in the initial 100 cycles, which are then continuously attenuated in the follow-up cycles. The result indicates that the uniformly distributed nano-sized CBP@TiP_2-C nanocomposite can shorten the diffusion path of lithium ion, which is conductive to the complete delithiation of alloyed phosphorus anode.[26, 27] Compared to the electrochemical performance of CBP@TiP_2-C and CBP-TiP_2-C electrodes, the CBP-TiP_2-C electrode exhibits a slightly worse electrochemical property. The result suggests that the *in-situ* fabricating CBP@TiP_2 composite process can make TiP_2 uniformly distribute into BP matrix and

enhance the interaction between each other, thus promoting the utilization of BP and the kinetics of electrochemical reaction.

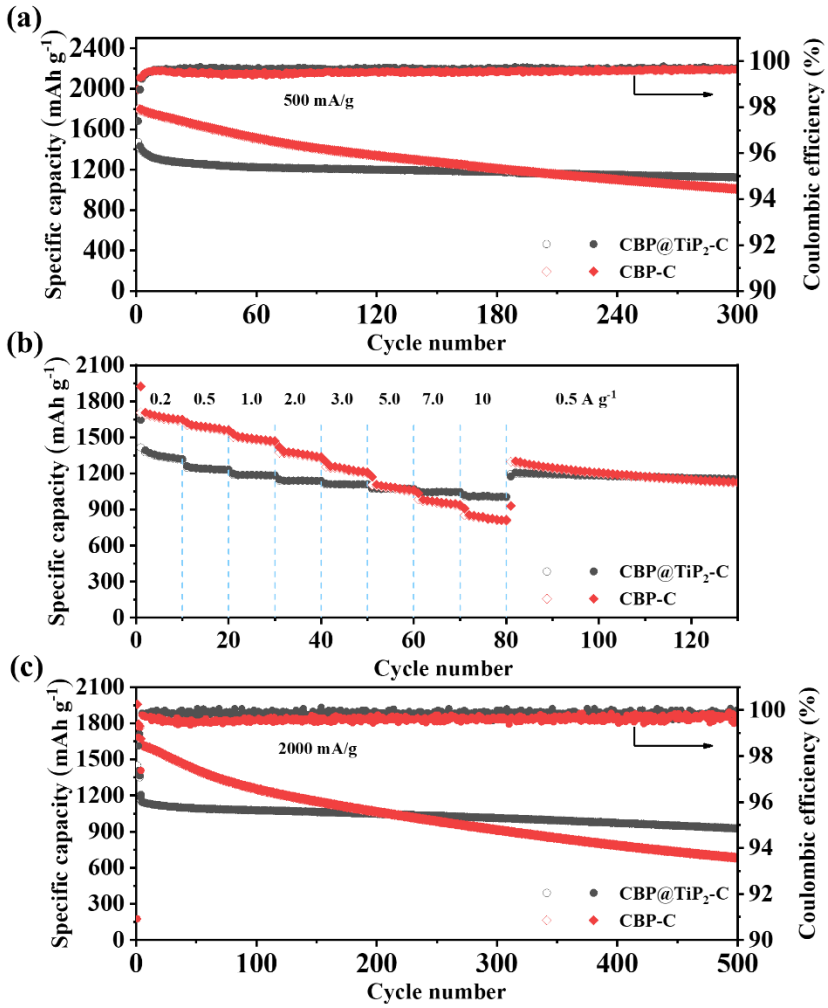

Fig. 3 The electrochemical performance of CBP@TiP_2-C and CBP-C electrodes. a) Cycle performances at 500 mA g^{-1}, b) rate capabilities, c) long cycle performance at 2000 mA g^{-1} with initial three cycles at 200 mA g^{-1}.

3.3 Reaction kinetics

Fig. 4a and 4c show the CV profiles of the CBP@TiP_2-C and CBP-C at various scan rates between 0.2 to 1.5 mV s^{-1} to investigate the kinetics mechanisms of the electrochemical reaction. The degree of capacitive effect can be obtained based on the relationship between current (i) and scan rate (v) stated by the equation, $i = av^b$, where

a and *b* are both constants. It has been reported that *b* approaching 0.5 relates to the diffusion-controlled process, while the surface capacitive-controlled process would be suggested when *b* is close to 1.0. [34, 35] Based on the anodic and cathodic peaks, *b*-values are determined by the linearly fitting the Log (*i*) vs Log (*v*) plots to be ~ 0.7 for both CBP@TiP_2-C and CBP-C electrodes, as shown in Fig. 4b and 4d. These results demonstrate the kinetics of both electrodes is controlled by the diffusion and pseudocapacitive processes and dominated by the diffusion-controlled process. In addition, the *b*-values of CBP-C electrode, especially in the anodic process, are smaller than that of CBP@TiP_2-C electrode, indicating the unfavored diffusion kinetics process.

EIS result has been evaluated to further investigate the reaction kinetics of these two electrodes. Fig. 4e shows the Nyquist plots of CBP@TiP_2-C and CBP-C electrodes at 2.0 V after 100 cycles. The spectra consist of the SEI resistance (R_f), charge transfer resistance (R_{ct}), and Li^+ diffusion process. The values can be calculated by the equivalent circuit (Fig. 4e). The CBP@TiP_2-C electrode has a lower R_f and R_{ct} parameters than the CBP-C electrode after cycling, which exhibits the stable electrode/electrolyte interface and fast electrode reaction kinetics. Furthermore, the ionic diffusion coefficient can be calculated by the Warburg coefficient σ, which is the slope of the plot between Z_{re} and $\omega^{-1/2}$ in Fig. 4f.[11] The CBP@TiP_2-C electrode shows a smaller σ value, demonstrating the superior Li^+ diffusion coefficient in active material. Above results demonstrates that the TiP_2 can decrease the Li^+ diffusion energy barrier and effective promote the Li^+ migration inside the active particles.

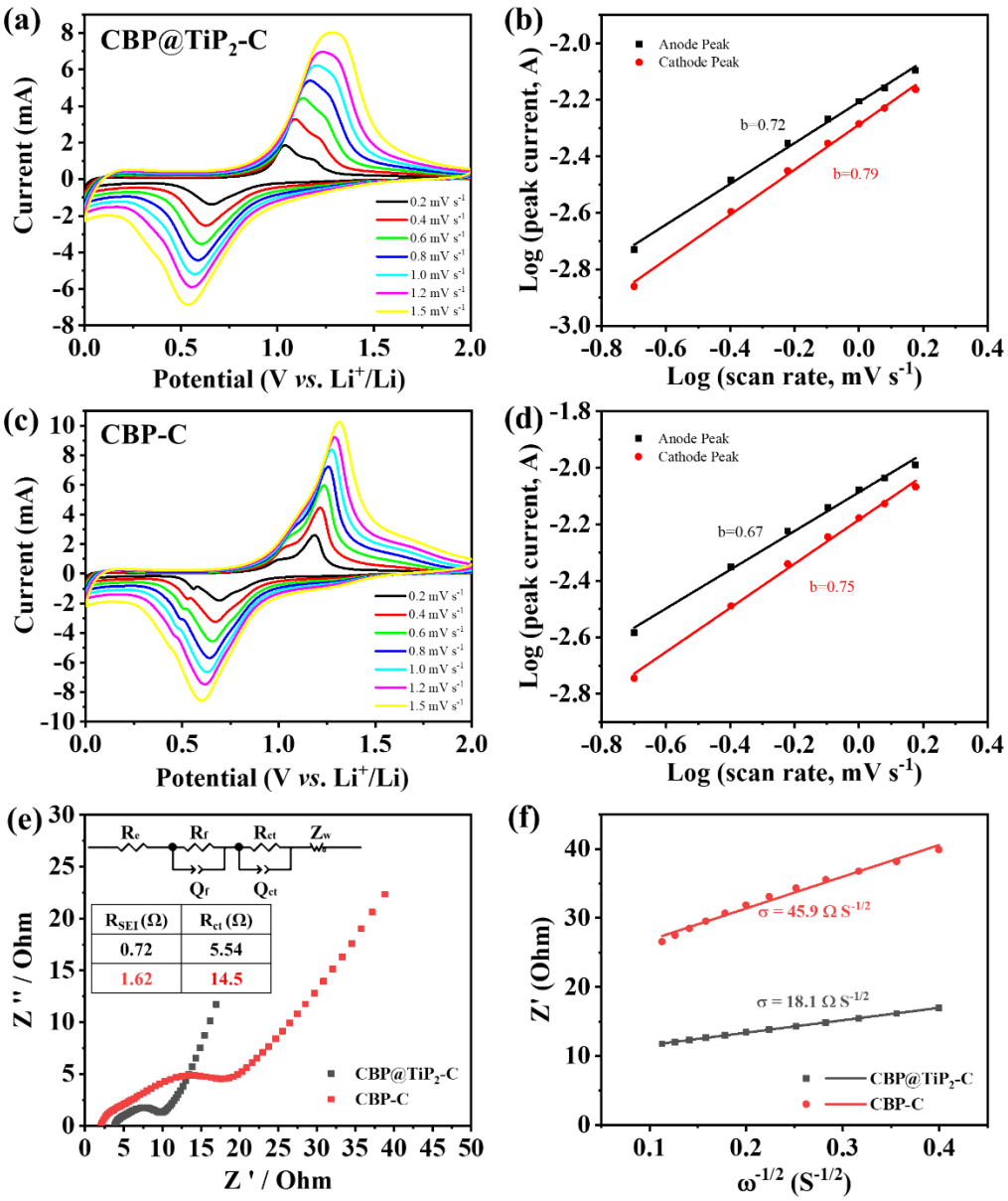

Fig. 4 Kinetic analysis of CBP@TiP_2-C and CBP-C electrodes for lithium storage. a) and c) CV curves at various scan rates, b) and d) relationship peak current against scan rate, e) electrochemical impedance spectra after 100 cycles at charge states of 2.0 V, f) relationship between Z_{re} and $\omega^{-1/2}$.

3.4 Electrochemical reaction mechanisms

To further investigate the phase evolution of the CBP@TiP_2-C electrode during electrochemical reaction, ex-situ TEM images at different voltage states were obtained and analyzed. Fig. 5a-c gives the HRTEM images of the CBP@TiP_2-C electrode after

initial discharged to 0.01 V, showing that the black phosphorus and TiP_2 phases are disappeared and converted to Li_3P and Li_yTiP_4 phases ($y < 11$, and the phase isostructural with Li_9TiP_4).[23] As indexed in Fig. 5a-c, the lattice frings of 0.322 nm are correspongded to (101) planes of the Li_3P phase, and the lattice frings of 0.21 and 0.298 nm are ascribed to (220) and (200) planes of Li_yTiP_4. In addtion, Fig. 5d-f show the HRTEM images of CBP@TiP_2-C electrode after initial charged to 2.0 V. At this higher votage level, no nanocrystalline BP, Li_yTiP_4 and TiP_2 phases are found, suggesting that the Li_3P phase is transferred to the amorphous phosphorus and the cubic Li_yTiP_4 phase loss its long range order for convertng to the amorphous TiP_4 with tetrahedral symmetry.[23] Besides, some nanocrystallites with lattice frings of 0.256 and 0.224 nm can be found among the amorphous matrix, which are ascribed to the (100) and (101) planes of Ti. With the Li^+ inserting into TiP_2, the orthorhombic TiP_2 phase can be tranferred to the cubic Li_yTiP_4 phase with the extrusion of excess Ti from the cubic phase.[23] Noticeably, the existence of Ti can improve electronic transmission within the composites. During the second discharge state to 0.01 V, the nanocrystalline LiP_3 and Li_yTiP_4 are re-appeared (as shown in Fig. 5g-i), indacting the reversible electrochemical reaction.

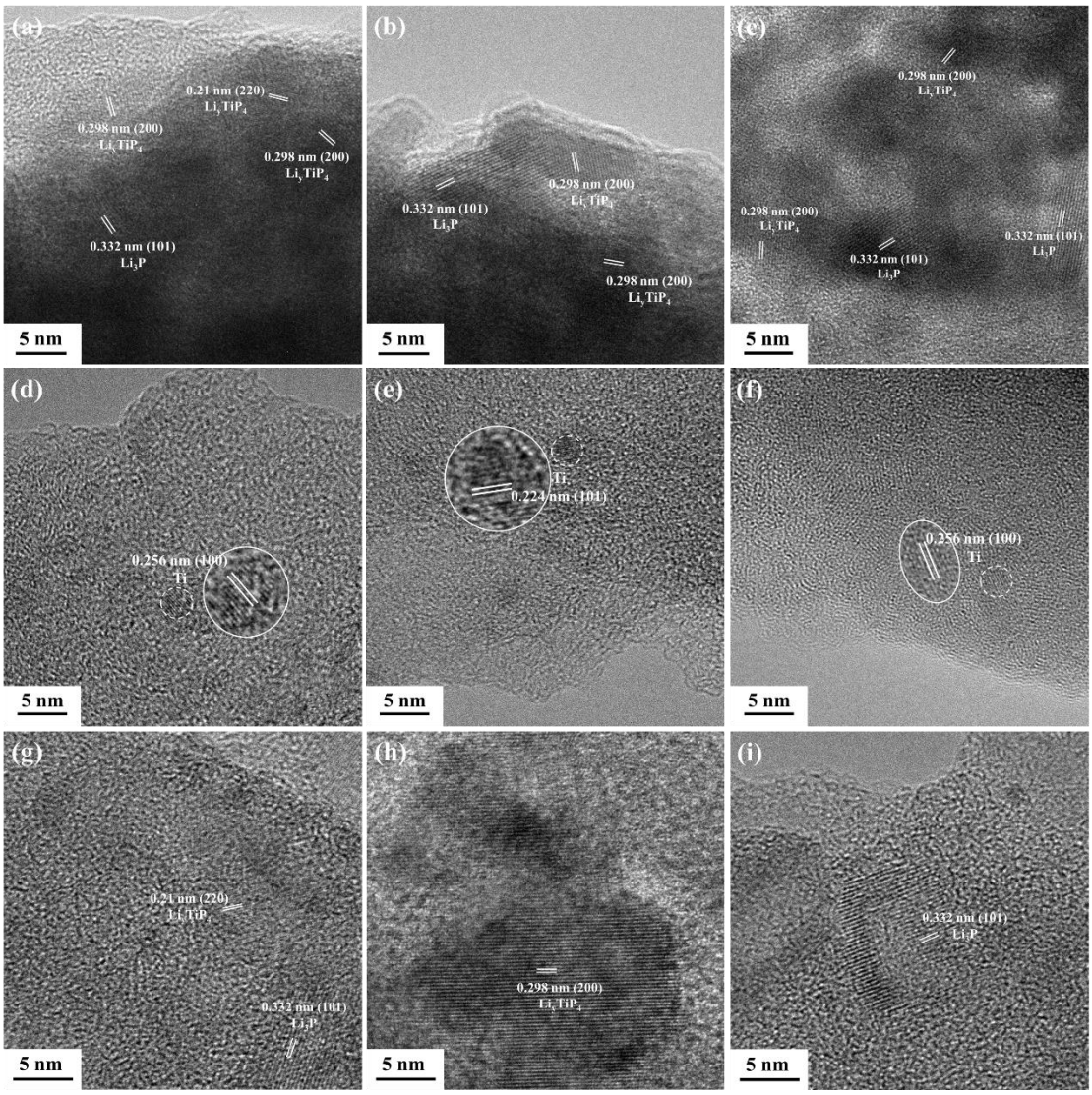

Fig. 5 Structure evolution of CBP@TiP_2-C electrode during cycling examined by ex-situ HRTEM. a-c) Initial discharged to 0.01 V, d-f) initial charged to 2.0 V, g-i) second discharged to 0.01 V.

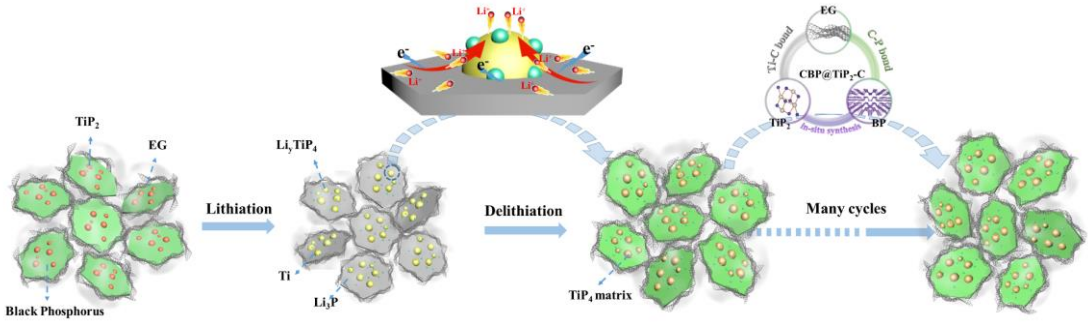

Fig. 6 Schematic illustration of the electrochemical reaction mechnism of CBP@TiP_2-C electrode.

Based on the above phase evolution results, a schematic illustration of the

electrochemical reaction mechnism of the CBP@TiP_2-C electrode is proposed as shown in Fig. 6. After the initial discharge process, TiP_2 tranfers into Li_yTiP_4 with high ionic conductivity, which can facilitate the Li^+ migration, and the *in-situ* extrudes excess Ti can enhance the electronic transmission within the composite. During the charge process, the Li_yTiP_4 can reduce the diffusion energy barrier of Li^+ and accelerate the Li^+ extraction from LiP_3. Besides, the fromed chemical bonds (P-C and Ti-C) can strengthen the contact among different components, thus ensuring the excellent electric contact within the material, and enhancing the structural stability during the lithiation/delithiation cycles. Therefore, an excellent cycling stability and rate performance can be achieved in our in situ synthesised CBP@TiP_2-C nanocomposite.

4. Conclusions

In the present work, a CBP@TiP_2-C nanocomposite has been synthesized by two-step high-energy ball milling for the high-rate performance LIB anode. During the *in-situ* ball milling process, more specifically, we have examined that the conductive TiP_2 nanocrystals can be uniformly distributed into BP matrix, which significantly promote the contact between BP, thus effectively enhancing the electronic and ionic conductivities of active particles. The electronic transmission can also be enhanced by the *in-situ* extrude excess nanocrystalline Ti. Moreover, the stable cubic Li_yTiP_4 phase upon lithiation can act as a buffer matrix to alleviate the stress form LiP_3. Furthermore, the formed Ti-C and P-C chemical bonds can improve the contact among these different components, thereby ensuring an excellent electric contact within the material and stable structure of composites. The outer carbon matrix can improve the electronic

conductivity of active composite, buffer the volume change, form a stable electrode/electrolyte interface. As a result, the CBP@TiP_2-C nanocomposite electrode displays a high rate reversible capacity of 1007.4 mAh g^{-1} at 10.0 A g^{-1}, and an ultra-durable cyclic life with a high reversible capacity of 925.6 mAh g^{-1} after 500 cycles at 2 A g^{-1}. The simple scalable synthesis approach in the present work will provide a new strategy to develop the high-rate performance of BP-based anode nanocomposites for the practical applications in high power density LIBs. Moreover, the one step *in-situ* ball milling synthesis technology can be extensively applied for synthesizing other BP@Metal phosphides.

Acknowledgments

This work was financially supported by the Foundation for Innovative Research Groups of the National Natural Science Foundation of China (No. NSFC51621001), National Natural Science Foundation of China Projects (Nos. 51771075 and 51971187).

Reference

[1] A. Manthiram, J. Phys. Chem. Lett., 2 (2011) 176-184.

[2] S. Goriparti, E. Miele, F. De Angelis, E. Di Fabrizio, R.P. Zaccaria, C. Capiglia, J. Power Sources, 257 (2014) 421-443.

[3] C.M. Park, H.J. Sohn, Adv. Mater., 19 (2007) 2465-2468.

[4] X.Y. Li, G. Chen, Z.Y. Le, X.R. Li, P. Nie, X.Y. Liu, P.C. Xu, H.B. Wu, Z. Liu, Y.F. Lu, Nano Energy, 59 (2019) 464-471.

[5] Y.M. Sun, L. Wang, Y.B. Li, Y.Z. Li, H.R. Lee, A. Pei, X.M. He, Y. Cui, Joule, 3

(2019) 1080-1093.

[6] H. Liu, S.X. Zhang, Q.Z. Zhu, B. Cao, P. Zhang, N. Sun, B. Xu, F. Wu, R.J. Chen, J. Mater. Chem. A, 7 (2019) 11205-11213.

[7] Y. Wu, F.F. Xing, R. Xu, X.L. Cheng, D.J. Li, X.F. Zhou, Q.B. Zhang, Y. Yu, J. Mater. Chem. A, 7 (2019) 8581-8588.

[8] Y. Liu, A. Zhang, C. Shen, Q. Liu, X. Cao, Y. Ma, L. Chen, C. Lau, T.C. Chen, F. Wei, C. Zhou, ACS Nano, 11 (2017) 5530-5537.

[9] J. Zhou, X. Liu, W. Cai, Y. Zhu, J. Liang, K. Zhang, Y. Lan, Z. Jiang, G. Wang, Y. Qian, Adv. Mater., (2017) 1700214.

[10] W.C. Chang, K.W. Tseng, H.Y. Tuan, Nano Lett., 17 (2017) 1240-1247.

[11] Z.L. Li, H.L. Zhao, P.P. Lv, Z.J. Zhang, Y. Zhang, Z.H. Du, Y.Q. Teng, L.N. Zhao, Z.M. Zhu, Adv. Funct. Mater., 28 (2018) 1605711.

[12] F.C. Zhou, L.Z. Ouyang, J.W. Liu, X.S. Yang, M. Zhu, J. Power Sources, 449 (2020) 227549.

[13] S. Liu, J. Feng, X. Bian, J. Liu, H. Xu, Y. An, Energy Environ. Sci., 10 (2017) 1222-1233.

[14] M. Ihsan-Ul-Haq, H. Huang, J. Cui, S. Yao, J. Wu, W.G. Chong, B. Huang, J.-K. Kim, J. Mater. Chem. A, 6 (2018) 20184-20194.

[15] Y. Xu, B. Peng, F.M. Mulder, Adv. Energy Mater., 8 (2018) 1701847.

[16] Z.-Z. Luo, Y. Zhang, C. Zhang, H.T. Tan, Z. Li, A. Abutaha, X.-L. Wu, Q. Xiong, K.A. Khor, K. Hippalgaonkar, J. Xu, H.H. Hng, Q. Yan, Adv. Energy Mater., 7 (2017) 1601285.

[17] X. Wang, H.M. Kim, Y. Xiao, Y.K. Sun, J. Mater. Chem. A, 4 (2016) 14915-14931.

[18] F.C. Zhou, L.Z. Ouyang, M.Q. Zeng, J.W. Liu, H. Wang, H.Y. Shao, M. Zhu, J. Alloys Compd., 784 (2019) 339-346.

[19] H. Jin, S. Xin, C. Chuang, W. Li, H. Wang, J. Zhu, H. Xie, T. Zhang, Y. Wan, Z. Qi, W. Yan, Y.R. Lu, T.S. Chan, X. Wu, J.B. Goodenough, H. Ji, X. Duan, Science, 370 (2020) 192-197.

[20] M.P. Bichat, F. Gillot, L. Monconduit, F. Favier, M. Morcrette, F. Lemoigno, M.L. Doublet, Chem. Mater., 16 (2004) 1002-1013.

[21] F. Gillot, L. Monoconduit, M. Morcrette, M.L. Doublet, L. Dupont, J.M. Tarascon, Chem. Mater., 17 (2005) 3627-3635.

[22] F. Gillot, M.P. Bichat, F. Favier, M. Morcrette, M.L. Doublet, L. Monconduit, Electrochim. Acta, 49 (2004) 2325-2332.

[23] S.-g. Woo, J.-H. Jung, H. Kim, M.G. Kim, C.K. Lee, H.-J. Sohn, B.W. Cho, J. Electrochem. Soc., 153 (2006) A1979-A1983.

[24] F. Zhou, X.-S. Yang, J. Liu, J. Liu, R. Hu, L. Ouyang, M. Zhu, J. Power Sources, 485 (2021) 229337.

[25] S.-O. Kim, A. Manthiram, Chem. Mater., 28 (2016) 5935-5942.

[26] D. Rehnlund, F. Lindgren, S. Böhme, T. Nordh, Y. Zou, J. Pettersson, U. Bexell, M. Boman, K. Edström, L. Nyholm, Energy Environ. Sci., 10 (2017) 1350-1357.

[27] C. Peng, H. Chen, G. Zhong, W. Tang, Y. Xiang, X. Liu, J. Yang, C. Lu, Y. Yang, Nano Energy, 58 (2019) 560-567.

[28] M. Zhang, L.Z. Ouyang, M. Zhu, F. Fang, J.W. Liu, Z.W. Liu, J. Mater. Chem. A,

8 (2020) 443-452.

[29] J. Sun, G. Zheng, H.W. Lee, N. Liu, H. Wang, H. Yao, W. Yang, Y. Cui, Nano Lett., 14 (2014) 4573-4580.

[30] W.-J. Li, S.-L. Chou, J.-Z. Wang, H.-K. Liu, S.-X. Dou, J. Mater. Chem. A, 4 (2016) 505-511.

[31] Y.M. Sun, X.L. Hu, W. Luo, F.F. Xia, Y.H. Huang, Adv. Funct. Mater., 23 (2013) 2436-2444.

[32] Q. Huang, S. Tian, D. Zeng, X. Wang, W. Song, Y. Li, W. Xiao, C. Xie, ACS Catal., 3 (2013) 1477-1485.

[33] T. Yuan, J. Ruan, C. Peng, H. Sun, Y. Pang, J. Yang, Z.-F. Ma, S. Zheng, Energy Storage Mater., 13 (2018) 267-273.

[34] V. Augustyn, J. Come, M.A. Lowe, J.W. Kim, P.L. Taberna, S.H. Tolbert, H.D. Abruna, P. Simon, B. Dunn, Nat. Mater., 12 (2013) 518-522.

[35] D. Chao, P. Liang, Z. Chen, L. Bai, H. Shen, X. Liu, X. Xia, Y. Zhao, S.V. Savilov, J. Lin, Z.X. Shen, ACS Nano, 10 (2016) 10211-10219.

[36] F.T.L. Muniz, M.A.R. Miranda, C.M. dos Santos, J.M. Sasaki, Acta Crystallographica a-Foundation and Advances, 72 (2016) 385-390.

[37] L. Zhao, Y.B. He, C.F. Li, K.L. Jiang, P. Wang, J.B. Ma, H.Y. Xia, F.Y. Chen, Y.B. He, Z. Chen, C.H. You, F.Y. Kang, J. Mater. Chem. A, 7 (2019) 24356-24365.

[37] Q. Xu, J.K. Sun, F.S. Yue, J.Y. Li, G. Li, S. Xin, Y.X. Yin, Y.G. Guo, ACS Appl. Mater. Interfaces, 10 (2018) 30479-30486.

In-situ introducing TiP_2 nanocrystals in black phosphorus anode to promote high rate-capacity synergy

Fengchen Zhou[a], Xu-Sheng Yang[c,d*], Jiangwen Liu[a], Jun Liu[a], Renzong Hu[a], Liuzhang Ouyang[a,b**], Min Zhu[a]

[a] School of Materials Science and Engineering, Guangdong Provincial Key Laboratory of Advanced Energy Storage Materials, South China University of Technology, Guangzhou, 510641, China. Email: meouyang@scut.edu.cn

[b] China-Australia Joint Laboratory for Energy & Environmental Materials, Key Laboratory of Fuel Cell Technology of Guangdong Province, Guangzhou, 510641, China
[c] Advanced Manufacturing Technology Research Centre, Department of Industrial and Systems Engineering, The Hong Kong Polytechnic University, Hung Hom, Kowloon, Hong Kong, China. Email: xsyang@polyu.edu.hk

[d] Hong Kong Polytechnic University Shenzhen Research Institute, Shenzhen 518057, China

[*]Corresponding authors.
[a**] E-mail: meouyang@scut.edu.cn, (L. Ouyang)

[c*] E-mail: xsyang@polyu.edu.hk, (X. Yang)

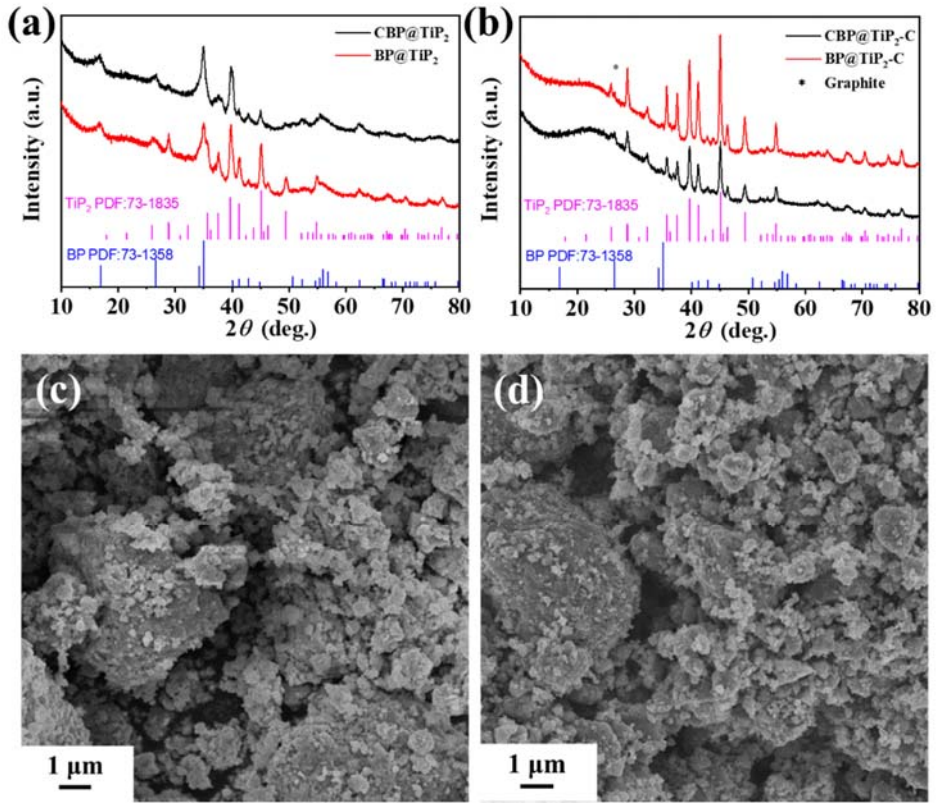

Fig. S1 The XRD patterns of a) CBP@TiP_2 and BP@TiP_2 composites, b) BP@TiP_2 and BP@TiP_2-C composites. The SEM images of c) BP@TiP_2, and d) BP@TiP_2-C.

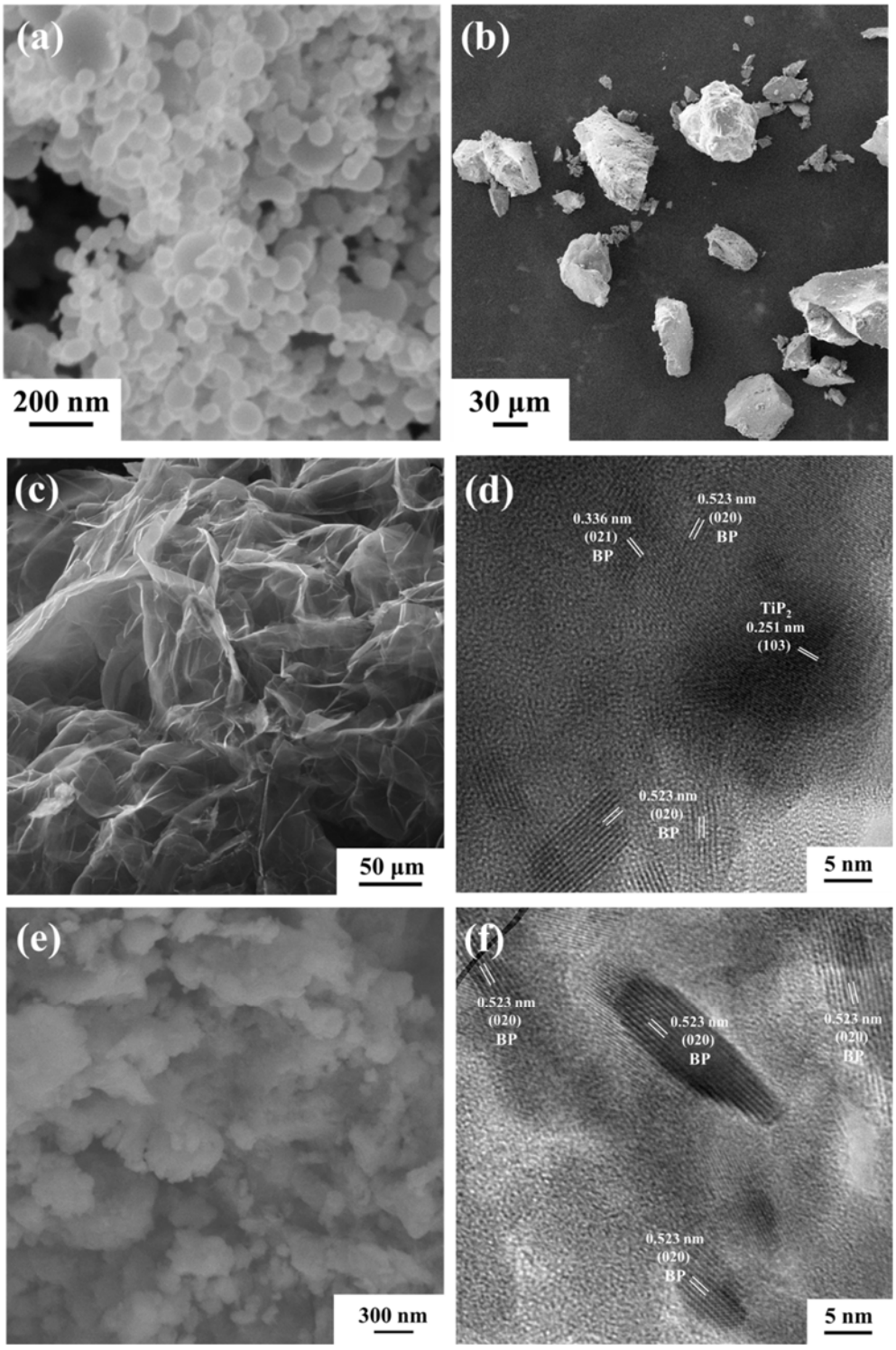

Fig. S2 The SEM images of a) Ti power, b) raw red P, c) EG, and e) CBP. TEM images of d) CBP@TiP_2 and e) CBP.

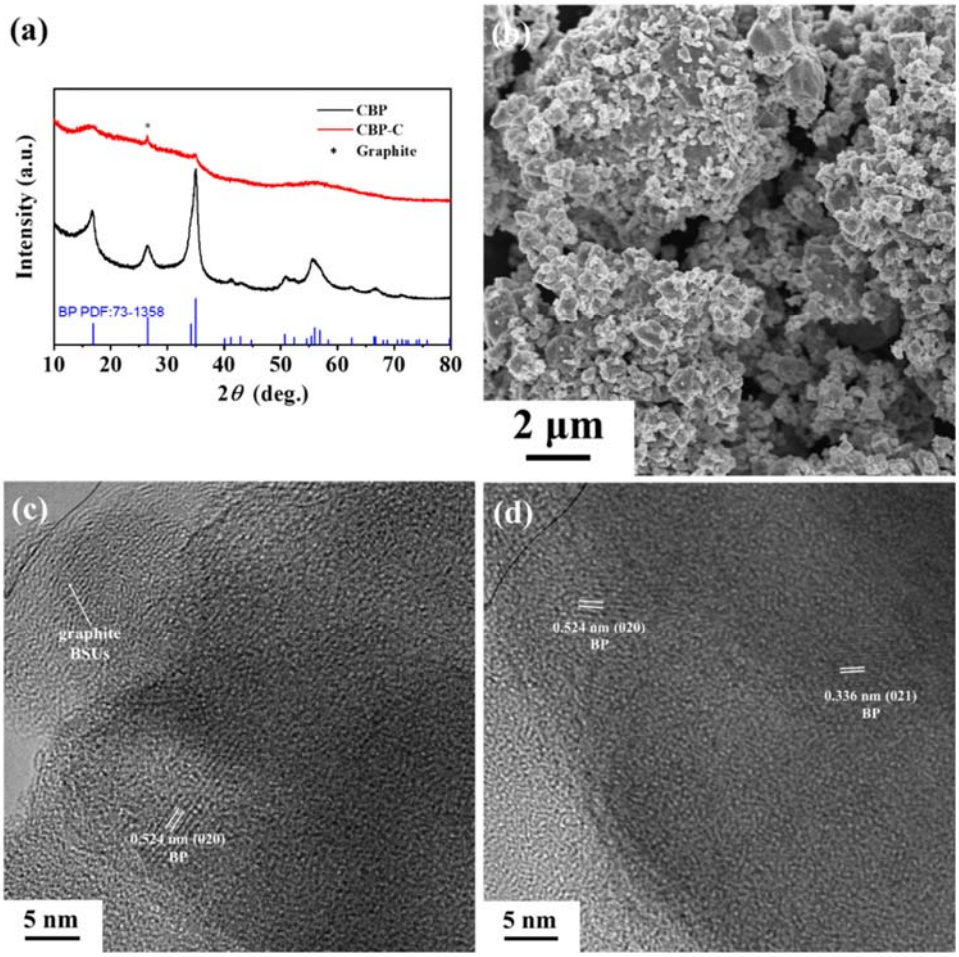

Fig. S3 a) The XRD patterns of CBP and CBP-C composites. b) The SEM image of CBP-C. c, d) HRTEM images of CBP-C composites.

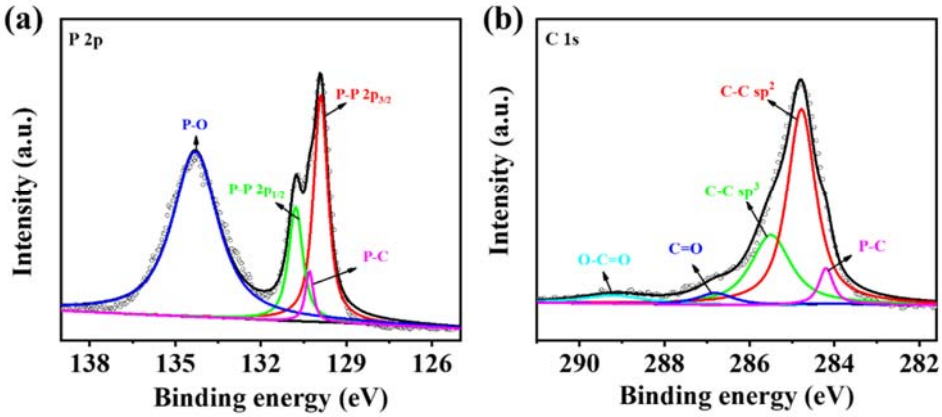

Fig. S4 High-resolution XPS spectrum of a) P 2p, and b) C 1s of CBP -C composite.

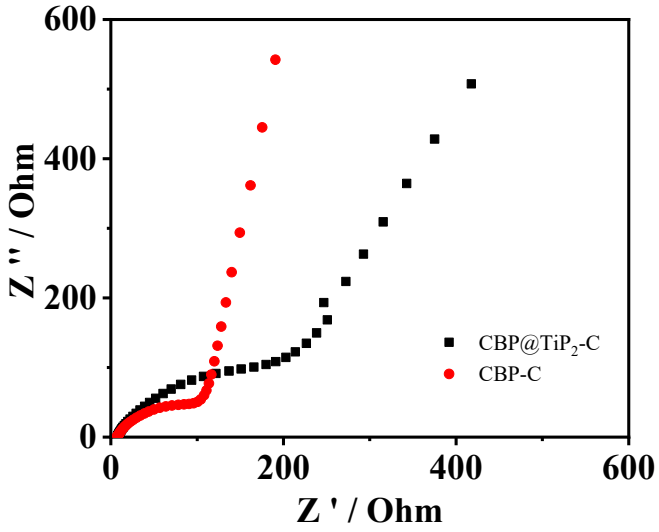

Fig. S5 The electrochemical impedance spectra of CBP@TiP_2-C and CBP-C electrodes before cycles.

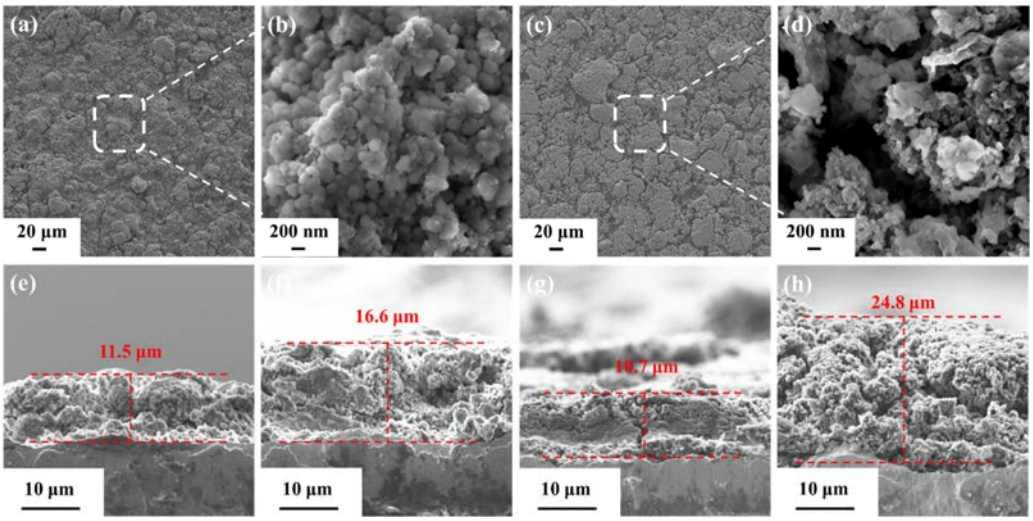

Fig. S6 SEM images of the top-view of a, b) CBP@TiP_2-C and c, d) CBP-C after cycling for 100 cycles at 1 A g^{-1}. Cross-sectional SEM images of e) CBP@TiP_2-C and g) CBP-C before cycling. Cross-sectional SEM images of f) CBP@TiP_2-C and h) CBP-C after cycling for 100 cycles at 1 A g^{-1}.

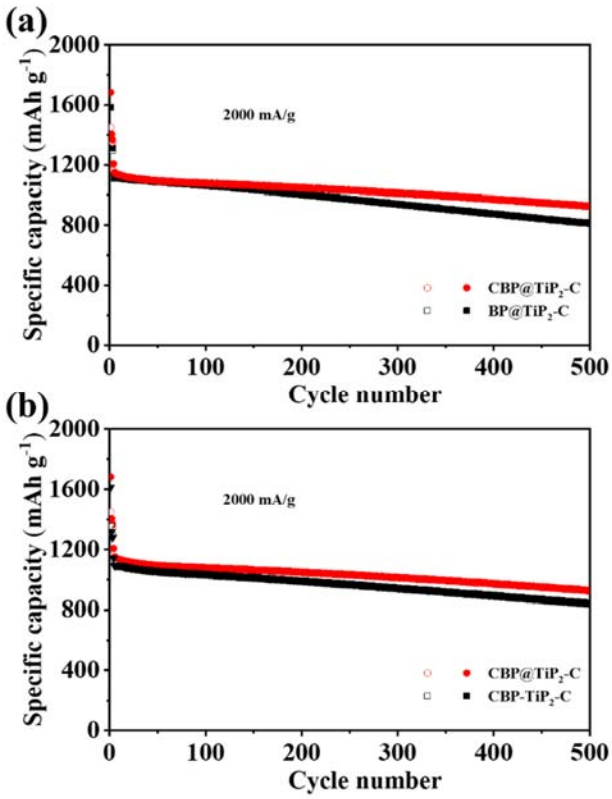

Fig. S7 Cycle performances of CBP@TiP_2-C, BP@TiP_2-C and CBP-TiP_2-C electrodes at 2000 mA g^{-1} with initial three cycles at 200 mA g^{-1}.

Table S1 Comparison of this work with previously reported P-based composites (the capacity based on the weight of composite).

Sample	Current densities	Reversible capacity	Initial coulombic efficiency	Cyclic performance	Reference
CBP@TiP_2-C	500 mA g^{-1}	1472.9 mAh g^{-1}	87.6%	Capacities of 1124.1 mAh g^{-1} after 300 cycles at 500 mA g^{-1}, ~925.6 mAh g^{-1} after 500 cycles at 2000 mA g^{-1} and 1007.4 mAh g^{-1} at 10.0 A g^{-1}	This work
rP-TiP_2-C	100 mA g^{-1}	1116 mAh g^{-1}	86.1%	Capacities of 1019 mAh g^{-1} after 100 cycles at 200 mA g^{-1} and 989 mAh g^{-1} at 1600 mA g^{-1}	[1]
BP@CNTs	100 mA g^{-1}	1381.4 mAh g^{-1}	90%	Capacities of 750 mAh g^{-1} after 100 cycles at 100 mA g^{-1}, 521.9 mAh g^{-1} afte 650 cycles at 500 mA g^{-1} and 380 mAh g^{-1} at 2500 mA g^{-1}	[2]
(BP-G)/PANI	260 mA g^{-1}	1650 mAh g^{-1}	76%	Capacities of 910 mAh g^{-1} after 2000 cycles at 2 A g^{-1} and 790 mAh g^{-1} after 2000 cycles at 5.2 A g^{-1}	[3]
RP/M-TiN/CNT	150 mA g^{-1}	1535.1 mAh g^{-1}		Capacities of 868.7 mAh g^{-1} after 850 cycles at 2.3 A g^{-1} and 360.3 mAh g^{-1} at 7.5 A g^{-1}	[4]
BP-TiO_2-C	500 mA g^{-1}	1331.1 mAh g^{-1}	84.19%	Capacities of ~1026 mAh g^{-1} after 200 cycles at 500 mAg^{-1} and 935.8 mAh g^{-1} after 300 cycles at 2000 mA g^{-1}	[5]
MXene/CNTs@P	130 mA g^{-1}	1687 mAh g^{-1}	77%	Capacities of 1039 mAh g^{-1} after 500 cycles at 130 mA g^{-1} and 722.5mAh g^{-1} at 2.6 A g^{-1}	[6]

FC@RP	130 mA g^{-1}	1608.7 mAh g^{-1}	57%	Capacities of 1380 mAh g^{-1} after 300 cycles at 130 mA g^{-1} and 1230 mAh g^{-1} after 1000 cycles at 2.6 A g^{-1}	[7]
BP-Gr	100 mA g^{-1}	920 mAh g^{-1}		Capacity of 402 after 500 cycles at 500 mA g^{-1}	[8]
P-SCNT composite	100 mA g^{-1}	1621.1 mAh g^{-1}	77%	Capacities of ~1398.5 mAh g^{-1} after 200 cycles at 100 mAg^{-1} and ~782 mAh g^{-1} after 3000 cycles at 2 A g^{-1}	[9]
P@HPCE-3/2	1000 mA g^{-1}	830 mAh g^{-1}	65.4%	Capacity of 636.7 after 100 cycles at 1000 mA g^{-1}	[10]
P@expanded-G50	100 mA g^{-1}	965.1 mAh g^{-1}	64%	Capacity of 1010 after 500 cycles at 100 mA g^{-1}	[11]
P/graphene	200 mA g^{-1}	1555 mAh g^{-1}	72%	Capacity of 1024 after 100 cycles at 200 mA g^{-1}	[12]
P@CNT	200 mA g^{-1}	1451.2 mAh g^{-1}	67%	Capacity of 960 after 120 cycles at 200 mA g^{-1}	[13]
PG-SPS	100 mA g^{-1}	1302 mAh g^{-1}	60.2%	Capacity of 725 after 200 cycles at 500 mA g^{-1}	[14]
BPQDs-NG	500 mA g^{-1}	1583 mAh g^{-1}	76.8%	Capacity of 1271 after 100 cycles at 500 mA g^{-1}	[15]
P-G	260 mA g^{-1}	1477 mAh g^{-1}	84%	Capacity of 898 after 300 cycles at 260 mA g^{-1}	[16]

References:

[1] S.-O. Kim, A. Manthiram, Chem. Mater., 28 (2016) 5935-5942.

[2] Y. Zhang, L. Wang, H. Xu, J. Cao, D. Chen, W. Han, Adv. Funct. Mater., 30 (2020) 1909372.

[3] H. Jin, S. Xin, C. Chuang, W. Li, H. Wang, J. Zhu, H. Xie, T. Zhang, Y. Wan, Z. Qi, W. Yan, Y.R. Lu, T.S. Chan, X. Wu, J.B. Goodenough, H. Ji, X. Duan, Science, 370 (2020) 192-197.

[4] X.P. Han, Z.X. Zhang, M.Y. Han, Y.R. Cui, J. Sun, Energy Storage Materials, 26 (2020) 147-156.

[5] F.C. Zhou, L.Z. Ouyang, J.W. Liu, X.S. Yang, M. Zhu, J. Power Sources, 449 (2020) 227549.

[6] S. Zhang, H. Liu, B. Cao, Q. Zhu, P. Zhang, X. Zhang, R. Chen, F. Wu, B. Xu, J. Mater. Chem. A, 7 (2019) 21766-21773.

[7] H. Liu, S.X. Zhang, Q.Z. Zhu, B. Cao, P. Zhang, N. Sun, B. Xu, F. Wu, R.J. Chen, J. Mater. Chem. A, 7 (2019) 11205-11213.

[8] L. Chen, G. Zhou, Z. Liu, X. Ma, J. Chen, Z. Zhang, X. Ma, F. Li, H.M. Cheng, W. Ren, Adv. Mater., 28 (2016) 510-517.

[9] T. Yuan, J. Ruan, C. Peng, H. Sun, Y. Pang, J. Yang, Z.-F. Ma, S. Zheng, Energy Storage Materials, 13 (2018) 267-273.

[10] T. Xu, D.H. Li, S. Chen, Y.Y. Sun, H.W. Zhang, Y.Z. Xia, D.J. Yang, Chem. Eng. J., 345 (2018) 604-610.

[11] J.F. Ruan, Y.P. Pang, S.N. Luo, T. Yuan, C.X. Peng, J.H. Yang, S.Y. Zheng, J. Mater. Chem. A, 6 (2018) 20804-20812.

[12] L. Sun, Y. Zhang, D. Zhang, Y. Zhang, Nanoscale, 9 (2017) 18552-18560.

[13] L. Sun, Y. Zhang, D. Zhang, J. Liu, Y. Zhang, Nano Research, 11 (2018) 2733-2745.

[14] Y. Zhang, H.W. Wang, Z.Z. Luo, H.T. Tan, B. Li, S.N. Sun, Z. Li, Y. Zong, Z.C.J. Xu, Y.H. Yang, K.A. Khor, Q.Y. Yan, Advanced Energy Materials, 6 (2016) 1600453.

[15] L. Pan, X.-D. Zhu, K.-N. Sun, Y.-T. Liu, X.-M. Xie, X.-Y. Ye, Nano Energy, 30 (2016) 347-354.

[16] Z. Yu, J. Song, M.L. Gordin, R. Yi, D. Tang, D. Wang, Adv Sci (Weinh), 2 (2015) 1400020.